The Astrophysical Journal, 961:231 (14pp), 2024 February 1 https://doi.org/10.3847/1538-4357/ad10a9

Enhanced Three-minute Oscillation above a Sunspot during a Solar Flare

Ya Wang[1,2], Lyndsay Fletcher[2,3], Sargam Mulay[2], Haisheng Ji[1,4], and Wenda Cao[5]
[1] Key Laboratory of Dark Matter and Space Astronomy, Purple Mountain Observatory, CAS, Nanjing, 210023, People's Republic of China; wangya@pmo.ac.cn
[2] SUPA School of Physics & Astronomy, University of Glasgow, G12 8QQ, UK
[3] Rosseland Centre for Solar Physics, University of Oslo, P.O. Box 1029 Blindern, NO-0315 Oslo, Norway
[4] School of Astronomy and Space Science, University of Science and Technology of China, Hefei, Anhui, 230026, People's Republic of China
[5] Big Bear Solar Observatory, New Jersey Institute of Technology, Big Bear City, CA 92314, USA
Received 2023 August 31; revised 2023 November 23; accepted 2023 November 27; published 2024 January 30

Abstract

Three-minute oscillations are a common phenomenon in the solar chromosphere above a sunspot. Oscillations can be affected by the energy release process related to solar flares. In this paper, we report on an enhanced oscillation in flare event SOL2012-07-05T21:42 with a period of around 3 minutes that occurred at the location of a flare ribbon at a sunspot umbral–penumbral boundary and was observed in both chromospheric and coronal passbands. An analysis of this oscillation was carried out using simultaneous ground-based observations from the Goode Solar Telescope at the Big Bear Solar Observatory and space-based observations from the Solar Dynamics Observatory. A frequency shift was observed before and after the flare, with the running penumbral wave that was present with a period of about 200 s before the flare coexisting with a strengthened oscillation with a period of 180 s at the same locations after the flare. We also found a phase difference between different passbands, with the oscillation occurring from high-temperature to low-temperature passbands. Theoretically, the change in frequency was strongly dependent on the variation of the inclination of the magnetic field and the chromospheric temperature. Following an analysis of the properties of the region, we found the frequency change was caused by a slight decrease of the magnetic inclination angle with respect to the local vertical. In addition, we suggest that the enhanced 3 minute oscillation was related to the additional heating, maybe due to the downflow, during the EUV late phase of the flare.

Unified Astronomy Thesaurus concepts: Active solar chromosphere (1980); Solar oscillations (1515); Solar flares (1496)

1. Introduction

Sunspot oscillations have been observed and studied for decades (Beckers & Tallant 1969). Three types of oscillations have been reported: the 5 minute oscillations at the photosphere (Ulrich 1970; Marmolino & Stebbins 1989), running penumbral waves (RPWs) (Nye & Thomas 1974; Priya et al. 2018), and 3 minute oscillations in the chromosphere above sunspots (Bogdan & Judge 2006). Five-minute oscillations are acoustic-type vibrations (p-modes), the origin of which is believed to be the standing acoustic waves in a subphotospheric cavity (Ulrich 1970). They are used to probe the solar interior. Observation shows that 5 minute oscillations with reduced amplitude in the umbra act as a filter in transmitting selected frequencies (Abdelatif et al. 1986). Braun et al. (1988) reported that the power of p-mode oscillation is absorbed in sunspots and the lifetime of high-degree p-modes may be reduced during solar activity. A spectroscopic study of sunspots investigated the power distribution for the frequency in a sunspot and the velocity power spectra showed a decrease within a period of 5 minutes in the sunspot (Balthasar et al. 1996). Observations presented by Kobanov & Makarchik (2004) also show the 5 minute p-mode oscillations propagate across the entire sunspot. Five-minute oscillations in fact show a broad distribution of frequencies, with a peak power at a period of roughly 5 minutes.

A significant phenomenon in the sunspot penumbra is RPWs. RPWs are described as chromospheric Hα velocity and intensity fronts that are observed to move out through the sunspot penumbra (Zirin & Stein 1972). Based on their visual pattern, many authors have provided evidence that RPWs are caused by field-aligned acoustic waves propagating up in the sunspot (e.g., Bloomfield et al. 2007). In this scenario, the pattern of delayed wave fronts gives rise to the apparent outward motion of the RPWs, which may also explain the large range of wave speeds. This scenario also indicates that RPWs can occur at the edge of a pore, and the existence of the penumbra is not necessary. Cho et al. (2015) presented observed wave properties of pores, which are similar to those in sunspots, using the Ca II 8542 Å and Hα lines. The results support the explanation of the observed wave as a slow magnetoacoustic wave propagating along the magnetic field in pores. The apparent horizontal motion can be explained by the projection effect caused by the inclination of the magnetic field with a canopy structure.

In this study, we mainly focus on the third type, 3 minute oscillations (Fleck & Schmitz 1991; Felipe 2019). It is generally believed that 3 minute oscillations are slow magnetoacoustic waves. For a low plasma β, where $\beta = 8\pi p/B^2 \ll 1$, the slow magnetoacoustic oscillation disturbs the magnetic field only slightly, and its behavior is the same as that of sound waves. In low-β plasma in a sunspot, slow magnetoacoustic waves are field-aligned compressive motions of the plasma, moving with the local sound speed along the magnetic field. Since the Alfvén speed exceeds the sound speed throughout the optically thin umbral atmosphere, and taking

into account the solar gravity, these fluctuations are classified as low-β slow magnetoacoustic-gravity (MAG) waves (Bel & Leroy 1977). A 3 minute oscillation is generally considered as being due to the leakage of higher frequencies in the 5 minute oscillation spectrum. Waves with frequencies higher than the local acoustic cutoff frequency are able to move upward from the photosphere through the chromosphere into the corona. For example, Centeno et al. (2006) reported that the 3 minute power observed at chromospheric heights comes directly from the photosphere by means of linear wave propagation between the levels of formation of the silicon and helium lines based on full Stokes vector IR spectropolarimetry.

Another explanation is that the chromosphere is an acoustic resonator, with a cavity formed between the photosphere and the transition region, which partially reflects the slow magnetoacoustic wave (e.g., Zhugzhda 2008; Botha et al. 2011). In this theory, parts of the solar p-mode spectrum with frequencies equal to or greater than the acoustic cutoff frequency transmit into the chromospheric cavity, which resonates at the acoustic cutoff frequency. However, as it is a leaky resonator, oscillations can propagate upward into the corona. The acoustic cutoff frequency is determined by $\omega \propto \cos\theta/\sqrt{T}$ (Fleck & Schmitz 1991), where θ is the angle between the magnetic field and the vertical, and T is the plasma temperature. Different temperature profiles of the sunspot's umbra would lead to different peaks in the spectrum of the chromospheric resonator, explaining the frequency variation in the sunspot oscillation. The existence of a chromospheric resonator is a matter of some debate (Felipe & Sangeetha 2020; Jess et al. 2020, 2021; Felipe et al. 2021) but opinion seems to be moving in its favor. Recent numerical modeling by Felipe & Sangeetha (2020) reveals that different profiles of the chromospheric temperature and density lead to variations in the cutoff frequency (that are quite different from analytic model predictions) so we would expect this to affect the observed frequency of oscillation. These authors also looked at the effect of changing the strength and inclination of the sunspot magnetic field. There is evidence of variation in the 3 minute oscillation spectrum across a sunspot. The frequency decreases in the horizontal direction from the sunspot center, due to the field lines being almost vertical in the center with gradually increasing inclination toward the edge of the sunspot (Sych & Nakariakov 2014). The $\cos\theta$ dependence of the cutoff frequency was verified numerically by Felipe & Sangeetha (2020) in regions where the temperature gradient was not too extreme.

On the other hand, flare quasiperiodic pulsations (QPPs) (Nakariakov & Melnikov 2009; Hayes et al. 2019; Zimovets et al. 2021) are a frequent phenomenon that has been known for over 50 yr. Flare QPPs are defined as a sequence of bursts of flare emission with similar time intervals between successive peaks. Typical periods of QPPs are in the range of a few seconds to a few minutes. It has been found that QPPs can appear in various phases of a solar flare, such as the pre-flare phase (Li et al. 2020), the impulsive phase, and the gradual phase (Zimovets et al. 2021). Various QPP mechanisms in solar flares have been proposed to work in different flares, leading to different types of QPPs. Several different physical processes may be responsible for the generation of QPPs, which can be summarized into the following three categories: (1) oscillatory processes (including MHD oscillations, QPPs triggered periodically by external waves, and dispersive wave trains) (e.g., Nakariakov et al. 2006), (2) self-oscillatory processes (including periodic spontaneous reconnection and coalescence of two magnetic flux tubes), and (3) autowave processes. A schematic illustration of the main models interpreting solar flare QPPs can be found in Kupriyanova et al. (2020). Many QPPs are identified based on the light curve of a region. Flare-related multiple periodic pulsations can be detected using multiple wavelengths and the generation mechanism is complicated (Li et al. 2021). Observational knowledge of the spatially resolved source region of flare QPPs is needed.

In recent years, some studies have reported a relationship between 3 minute oscillations and energetic events (e.g., Kosovichev & Sekii 2007; Sych et al. 2009; Milligan et al. 2017; Millar et al. 2021). Sych et al. (2009) provided observational evidence of the leakage of 3 minute oscillations into the corona along the coronal loops, and proposed that these are involved in triggering QPPs in the energy release. Millar et al. (2021) studied the variation of the location and period of chromospheric oscillations during a solar flare, and by comparing the pre-flare and post-impulsive behavior they provided evidence that the change in the magnetic environment caused by a solar flare can affect the oscillations. Milligan et al. (2017) studied the 3 minute oscillations in Lyα and LyC emission during an X-class flare finding evidence that compressible waves with a period around the acoustic cutoff are created when the chromosphere is impulsively disturbed. In order to understand the nature of 3 minute oscillations above a sunspot during flares, we require further study using high-resolution observations and magnetohydrodynamic (MHD) numerical simulations.

In this paper, we analyze a strong-intensity oscillation observed at high resolution in a flare ribbon at an umbral–penumbral boundary. The flare event, SOL2012-07-05T21:42, was an M1.8-class X-ray flare, other aspects of which have been studied from three perspectives. These are (1) the sunspot dynamics during the flare (Part I, Wang et al. 2016), (2) the origin and destination of multiple hot channels (Part II, Wang et al. 2018), and (3) the EUV late phase (Part III, Wang et al. 2018). We mentioned an apparent "back and forth" oscillation of the flare ribbon's position in Part I, while in Part III, we highlighted the presence of strong downflows in the region, including their influence on the loop, which we study in this work.

Here we study and discuss the enhanced 3 minute oscillation in multiple passbands at the sunspot's umbral and penumbral boundary, where the footpoint of the late phase loops and the flare ribbon arrives. We perform a joint analysis of data from ground-based and space-based instruments to characterize the oscillation properties before and after the flare, at wavelengths corresponding to emission from the deep chromosphere to coronal temperatures. In this way, we find the connection between waves in the chromosphere and the corona through direct comparison of the oscillation variations by studying their spatial and temporal properties both visually and using cross-correlation. Section 2 provides an overview of the active region, and we present our analysis and results in Section 3. The conclusions and discussion are presented in Section 4.

2. Data and Overview of the Active Region

The observational data in this paper are the same as those previously introduced in Wang et al. (2016, 2018, 2020). High-

resolution ground-based images were obtained in the He I 10830 Å narrow band (bandpass: 0.5 Å) from the Big Bear Solar Observatory (BBSO) with the 1.6 m aperture Goode Solar Telescope (GST) (Goode et al. 2010; Goode & Cao 2012). For the He I 10830 Å images, the pixel size is 0.″0875, the cadence is around 10 s, and the field of view (FOV) is about 90″ × 90″. High-resolution Hα images at the line center, 6563 Å, and in the −0.75 Å blue wing were also taken from BBSO/GST. For the Hα images, the pixel size is 0.″056. The cadence is about 34 s for the Hα line center and 10 s for the Hα blue wing. Long-duration good seeing conditions at BBSO and the high-order adaptive optics system are beneficial for obtaining consecutive diffraction-limited images lasting for hours. The seeing conditions were good on 2012 July 5, and NOAA Active Region (AR) 11515 (S17W37)[6] was selected as the observation target. The active region consisted of a sunspot that had a complex magnetic configuration of $\beta\gamma\delta$. The FOV of GST contained the western part of the active region, which was dominated by a positive magnetic field and surrounded by satellite sunspots with scattered negative fields. The Geostationary Operational Environment Satellite (GOES-15) recorded an M1.8-class X-ray flare originating from this active region at 21:37 UT. The flare peaked at 21:42 UT and ended at 22:30 UT. Based on the EUV-integrated light curves shown in Figure 2 of Wang et al. (2020), we identified three phases of the flare: the pre-flare phase (between 21:00 and 21:36 UT), the impulsive phase (between 21:37 and 21:45 UT), and the EUV late phase (between 21:55 and 22:30 UT). The EUV late phase is a second gradual-phase peak in the warm EUV irradiance, such as Fe XVI 335 Å (∼3 MK) discovered by Woods et al. (2011) using the Extreme Ultraviolet Variability Experiment instrument (Woods et al. 2012) on board the Solar Dynamics Observatory (SDO). The main sunspot associated with AR 11515 is shown in Figure 1, in the Hα blue wing −0.75 Å (panel (a)), Hα 6563 Å (panel (b)), and He I 10830 Å (panel (c)) passbands at 21:53 UT.

We studied this flare using UV/EUV images obtained from the Atmospheric Imaging Assembly instrument (AIA; Lemen et al. 2012) on board SDO (Pesnell et al. 2012) during the time interval when the ground-based data were available. AIA captures full-disk images of the solar disk (4096 × 4096 pixels) every 12 s in seven EUV passbands and every 24 s in two UV passbands with a spatial resolution of 1.″2 (a pixel size of 0.″6). The seven EUV passbands (O'Dwyer et al. 2010; Del Zanna 2013) are 94 Å (Fe XVIII, $\log T\,[\mathrm{K}] = 6.8$), 131 Å (Fe VIII, XXI, $\log T\,[\mathrm{K}] = 5.6,\ 7.0$), 171 Å (Fe IX, $\log T\,[\mathrm{K}] = 5.8$), 193 Å (Fe XII, XXIV, $\log T\,[\mathrm{K}] = 6.2,\ 7.3$), 211 Å (Fe XIV, $\log T\,[\mathrm{K}] = 6.3$), 304 Å (He II, $\log T\,[\mathrm{K}] = 4.7$), and 335 Å (Fe XVI, $\log T\,[\mathrm{K}] = 6.4$). They are sensitive to the corona and transition region, except for 304 Å, which is sensitive to the chromosphere. In addition, UV images with 24 s cadence were obtained from the AIA 1600 and 1700 Å passbands. In the quiet Sun these channels are sensitive to the photosphere, chromosphere, and transition region. The flare excess emission in the 1600 Å channel is dominated by C IV ($\log T\,[\mathrm{K}] = 5.0$) and the Si continuum, and that in the 1700 Å channel by C I ($\log T\,[\mathrm{K}] = 4.2$) and He II (Simões et al. 2019).

The near-simultaneous images in the UV and EUV passbands are shown at 21:53 UT in Figure 1 (panels (d)–(l)). Note that the FOV shown in the AIA 1600 and 1700 Å images is bigger than the FOV shown in other panels in this figure. The red boxed region highlighted in panel (l) indicates the FOV shown in the Hα, He I, and EUV passbands. The sunspot is highlighted in panel (k) with white contours and the same contours are overplotted in the AIA 335 Å image in panel (j). Slit 1 (with length 10 Mm) is plotted in these panels, crossing the umbral–penumbral boundary of the sunspot. The region captured in this slit was further used to identify oscillations in the EUV passbands (see Section 3.1 and Figure 4). Slit 2 of length 20 Mm is shown in red color in panels (i)–(j), crossing both umbral–penumbral boundaries of the sunspot, where we identified RPWs (see Figure 3).

As previously analyzed (Wang et al. 2016, 2018, 2020), a large-scale filament rooted in the sunspot erupted and was accompanied by a coronal mass ejection. The three sets of loops, mutually confirmed by AIA imaging observations and the magnetic topology from nonlinear force-free field extrapolations, included a set of post-flare loops and two sets of late-phase loops (see Figures 3 and 4 in Wang et al. 2020). A main flare ribbon and a secondary flare ribbon were observed at around 21:42 UT (see Figure 1 in Wang et al. 2020). The EUV late phase dominated the gradual phase observed in the EUV passbands, especially the 335 Å passband, showing second peaks after the impulsive phase. During the flare, one of the flare ribbons swept into the sunspots and oscillated. Based on our previous studies, we identified three sets of loops in the region. Two of them were the post-flare loop and the EUV late-phase loop. The footpoints of both loop sets were at the location of oscillation. The late-phase loop connected the flaring site and a remote plage region, which was located at an asymmetric quadrupole magnetic field configuration. During the EUV late phase, downflowing plasma was observed, which collided with material in the low-lying atmosphere (see Figures 7 and 8 and the corresponding animation in Wang et al. 2020). In Part III (Wang et al. 2020), we proposed that this could be an additional heating mechanism of the EUV late-phase loops.

3. Analysis and Results

3.1. The Oscillation Phenomenon

During the impulsive phase of the flare the eastern branch of the two ribbons advanced rapidly into the sunspot and oscillated in position at the boundary between the umbra and penumbra. Figure 1 shows the ribbon position after the impulsive phase. The flare ribbon shows emission in all passbands except for the He I 10830 Å passband, where it is in absorption and shows up dark.

We first remarked on the oscillation of the ribbon position in the He I 10830 Å passband in Wang et al. (2016). To further investigate the oscillatory behavior, we took a small region, shown by the red box in Figure 1, panel (c), and obtained the He I time profile of the integrated intensity. The results are shown in Figure 2. The detrended intensity in this region of the ribbon presents significant oscillations, which can be characterized using a Morlet wavelet analysis (Torrence & Compo 1998). Panels (a1) and (a2) present the raw time series integrated over the red box shown in Figure 1, panel (c). The overlaid red curve in panel (a1) presents the slow-varying trend, and the detrended time series is shown in panels (b1) and (b2). Here, we use smoothing boxcars with widths of 5 minutes and 3 minutes for the raw light curves in panels (a1) and (a2),

[6] https://www.solarmonitor.org/?date=20120705

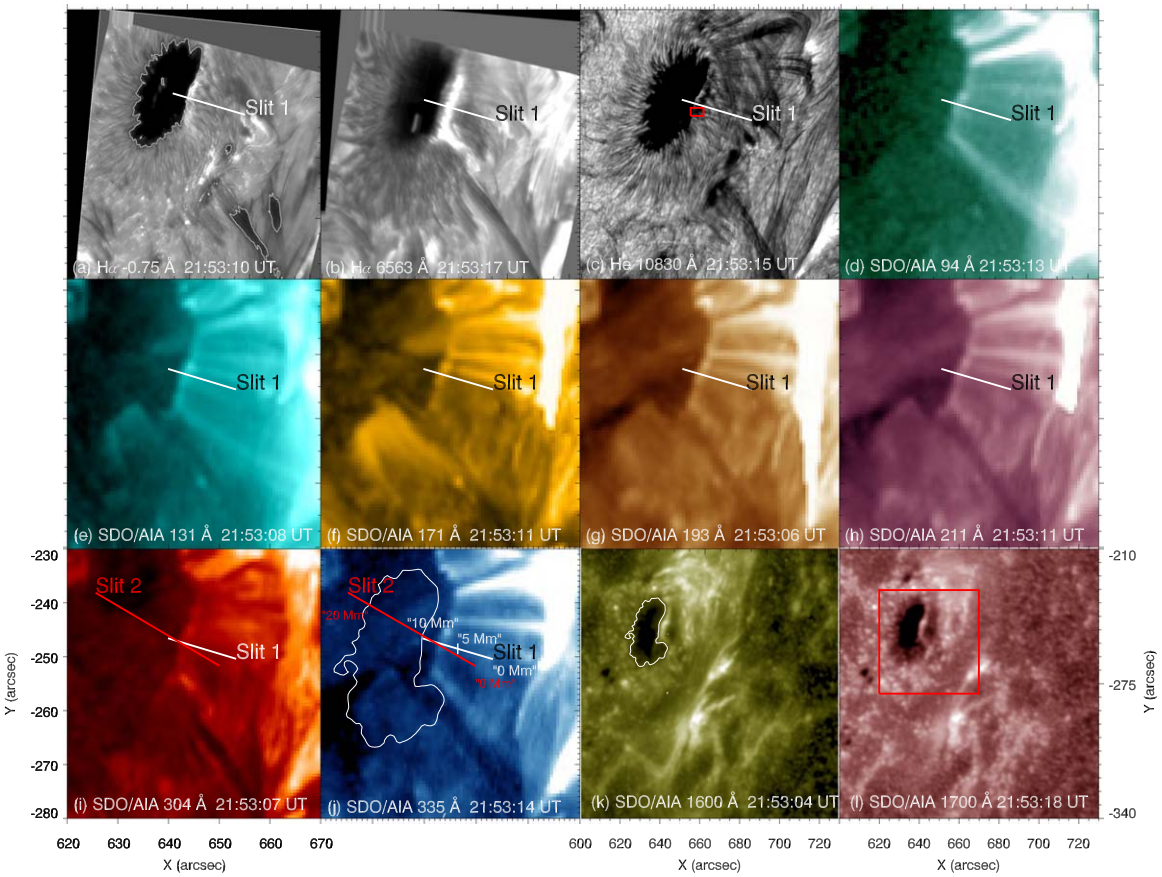

Figure 1. Panels (a)–(c): near-simultaneous images of the sunspot and the flare emission are shown at multiple wavelengths—Hα blue wing −0.75 Å, Hα 6563 Å, and He I 10830 Å—from BBSO/GST. The white contour in panel (a) represents the contour of the sunspot's umbra (for DN s^{-1} = 1000). The red box in panel (c) was used to create the intensity profiles in Figure 2. Panels (d)–(l): EUV and UV images obtained from the Atmospheric Imaging Assembly (AIA) passbands—94, 131, 171, 193, 211, 304, 335, 1600, and 1700 Å, respectively. The red boxed region in panel (l) represents the FOV for all the AIA EUV images shown in panels (d)–(j). The white (red) solid lines indicate slit 1 (slit 2), an artificial slit that was used to create the time–distance plots shown in Figure 4 (Figure 3). Slit 1's and slit 2's lengths are 10 and 20 Mm, respectively. The contour in panel (k) represents the outline of the sunspot (including the umbra and penumbra for an intensity of AIA 1600 Å = 75 DN s^{-1}) and we plot the same contour in panel (j). Please note, panels (k) and (l) have a different scale from the others.

respectively, to remove the large-scale trend. The low-frequency components are removed. Detrending is often utilized in time series before analysis of their period or frequency in order to strengthen the periodic signals in the raw time series (Auchère et al. 2016). We performed wavelet analysis for the detrended light curves (panels (b1) and (b2)). The parameter ω_0 for the Morlet wavelet was set to 6 by default. We preferred to use a small (the default) value in order to have a good time resolution, because of fast variation around the flare. The wavelet power spectra show a dominant period of 3–4 minutes, which is above the 95% significance level. The times of two microflares (which are regarded as two precursors) and the flare impulsive phase, respectively 21:20, 21:30, and 21:42 UT, are indicated with red arrows on the light curve. The first precursor and the impulsive phase correspond to dips in the light curve (Figure 2, panel (a2)). Compared with the pre-flare stage before 21:30 UT (Figure 2, panels (a1)–(c1)), the 3 minute oscillation is enhanced from 21:50 to 22:15 UT (Figure 2, panel (c2)), which is right in the EUV late phase of the flare. Additionally, a frequency shift occurs before and after the impulsive phase of the flare. We note first of all that the dominant period before 21:15 UT is about 5 minutes because the He I 10830 Å images at this time likely also include photospheric emission from the quiet Sun. Then, between 21:20 and 21:33 UT (after the first precursor) the dominant period is a chromospheric period of about 200 s. This decreases to 180 s between 21:50 and 22:15 UT. The interpretation will be described in detail in the following sections.

To compare the intensity oscillation in the sunspot's umbra and penumbra, and the oscillation before and after the flare, we made a slice across the sunspot (at the slit 2 location shown in red color in panels (i) and (j) of Figure 1) with a length of about 20 Mm and used this to create time–distance plots in the Hα 6563 Å and AIA 1700 and 304 Å passbands, which are shown in Figure 3. GST/Hα data is unavailable after 22:22 UT and SDO/AIA 1700 Å data is unavailable before 21:30 UT. For the AIA 1700 Å data, we cannot study the RPW before the flare due to lack of data. However, after the flare we can study the properties of the RPW that is clearly visible at 1700 Å on the other side of the sunspot.

In Figure 3 panel (a), we show the time–distance plot in the AIA 304 Å passband overlaid (as a green curve) with the X-ray fluxes observed by GOES-15 in the 1–8 Å channel. The extent of the umbral and penumbral boundaries is indicated by dotted green and white horizontal lines, respectively, in all images. We clearly observe the umbral wave (between 8 and 12 Mm) in the sunspot's umbra, propagating from the center of the umbra toward the penumbra, with a characteristic pattern like a stack of bowls. The edge of the bowls extends to the penumbra. In

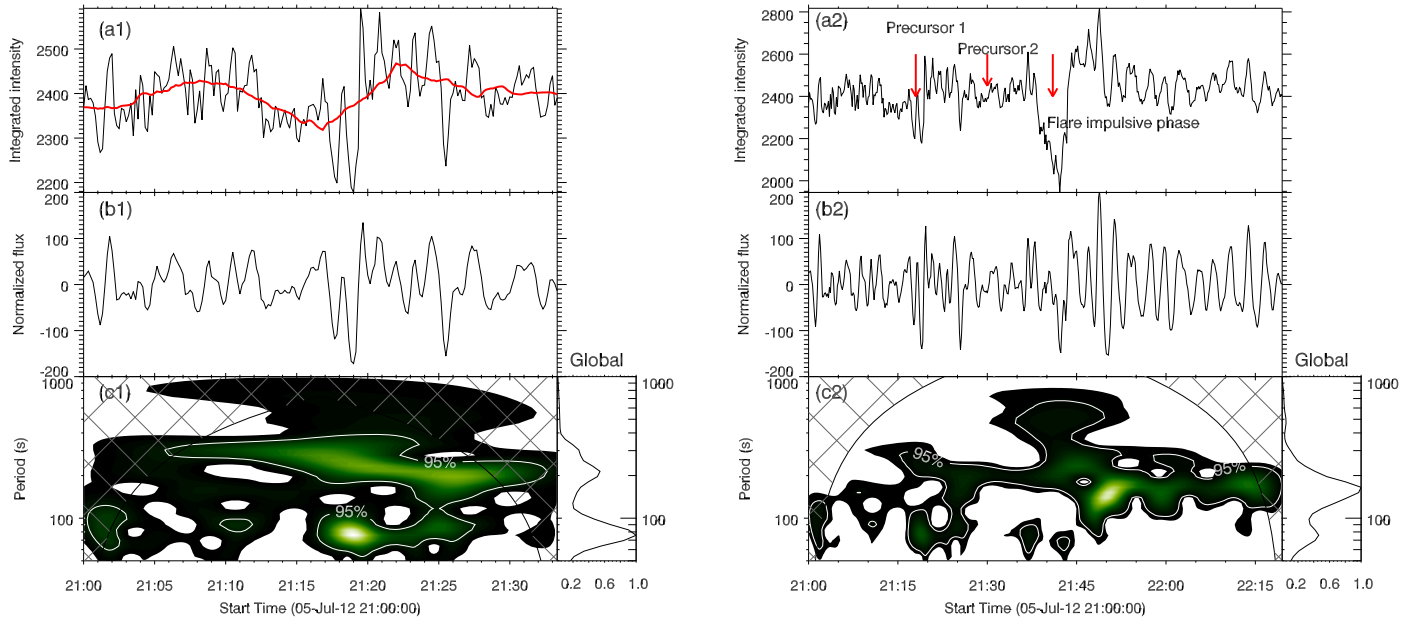

Figure 2. He I 10830 Å time profiles of the intensity integrated over the red boxed region shown in Figure 1 (panel (c)). They are plotted for the pre-flare phase from 21:00 to 21:33 UT (panels (a1)–(c1)) and over the whole event from 21:00 to 22:20 UT (panels (a2)–(c2)). The red curve overlaid on the profile shown in panel (a1) is the slow component for the time profile. The three arrows in panel (a2) indicate the times of the two precursors (21:20 and 21:30 UT) and the flare impulsive phase (21:42 UT), where the absorption reaches its trough. Panels (b1) and (b2) represent the fast component for the intensity obtained from the time profile in panels (a1) and (a2); panels (c1) and (c2) show the wavelet analysis of the power spectrum using the Morlet wavelet. The power is normalized. The white contour indicates the 95% confidence level and the bright region inside the white contour indicates a region with a greater than 95% confidence level for a white-noise process. Cross-hatched regions indicate the cone of influence, where the edge effect becomes important. The peak at around 80 s (panel (c1)) is produced by a microflare at ∼21:20 UT, which is regarded as the first precursor. The global wavelet power spectra are also shown.

the AIA 304 Å passband, we do not observe the RPWs between 21:00 and 21:40 UT. During the EUV late phase, we find that there is enhanced oscillation at the boundary between the sunspot's umbra and penumbra from ∼22:00 to ∼22:35 UT (the region is shown between two solid white lines). This is consistent with the enhanced signal of the 3 minute oscillation on the integrated light curve of the He I 10830 Å passband (see Figure 2).

In Figure 3 panel (b), we show the Hα 6563 Å time–distance plot and the RPW (observed as black and gray stripes between the two red horizontal lines running from 8 to 4 Mm during 21:00 to 21:20 UT) propagates at a speed of 10.2−18.1 km s^{-1} before the flare onset. The enhanced oscillation (shown by the two red horizontal lines during 22:00 to 22:20 UT) and the RPW (shown as two blue lines during 22:07 to 22:22 UT) coexist during the late phase of the flare. Figure A1 in the Appendix shows the coexistence of the two features. While a part of the RPW converts into oscillation during the EUV late phase, the other part of the wave maintains the same pattern as that before the flare.

In Figure 3 panel (c), we show the time–distance plot at 1700 Å. We observe the penumbral wave propagating on the other side of the sunspot (at ∼13 Mm between 21:50 and 22:20 UT). The propagation speeds are 14.7 to 27.8 km s^{-1} as found by linear fitting of the pattern of the motion. We also find an enhanced fluctuation at the opposite boundary between the sunspot's umbra and penumbra during the same period when the signal is seen in the 1700 Å passband (see black and white stripes around 5 Mm in panel (c) of Figure 3 during 21:50 to 22:30 UT). However, the observed fluctuation seems to be irregular.

We made slices along the direction of the oscillation to obtain the time–distance plots in Figure 4, i.e., at the position of slit 1 that is indicated by white lines in Figure 1 (panels (a)–(j)). The slices are almost perpendicular to the flare ribbon. In these time–distance plots (Figure 4), the dark region above 8.5 Mm corresponds to the sunspot's umbra and the bright region is emission from the late phase of the flare. The oscillation lasts for more than 1.5 hr, which covers the range of the EUV late phase. We observe at least seven oscillation pulses and they are indicated by number (1−7) in the 131 Å passband (Figure 4, panel (d)). By examining the imaging observations in the Hα 6563 Å and EUV passbands, we confirm that the intensity oscillation is unambiguously present in both the chromospheric and coronal passbands.

We obtained the intensity variation profiles for all AIA EUV, Hα, and He I passbands between 22:00 and 22:20 UT along the white horizontal lines indicated in Figure 4 and the results are shown in Figure 5. There are obvious time lags (phase differences) between each passband. We took the AIA 94 Å passband as a reference and obtained time lags in all AIA passbands using cross-correlation and the results are presented in Table 1. In addition, we took the AIA 304 Å passband as a reference and obtained time lags for the Hα and He I passbands and the results are summarized in Table 2. We found that the peak of the oscillation in the intensities occurs first in the high-temperature EUV passbands like 94 and 131 Å, and then in some of the cooler EUV passbands. Finally, it occurs in the chromospheric Hα 6563 Å line. However, the oscillatory behavior of the He I 10830 Å line is quite consistent with the AIA 304 Å passband (dominated by the He II line), rather than with the chromospheric Hα 6563 Å line because the formation of He I 10830 Å is complicated. He II 304 Å is singly ionized helium and He I 10830 Å corresponds to the transition between $1s2s\ ^3$S and $1s2s\ ^3$P of the helium triplet. For the formation mechanism of the helium triplet, the photoionization then

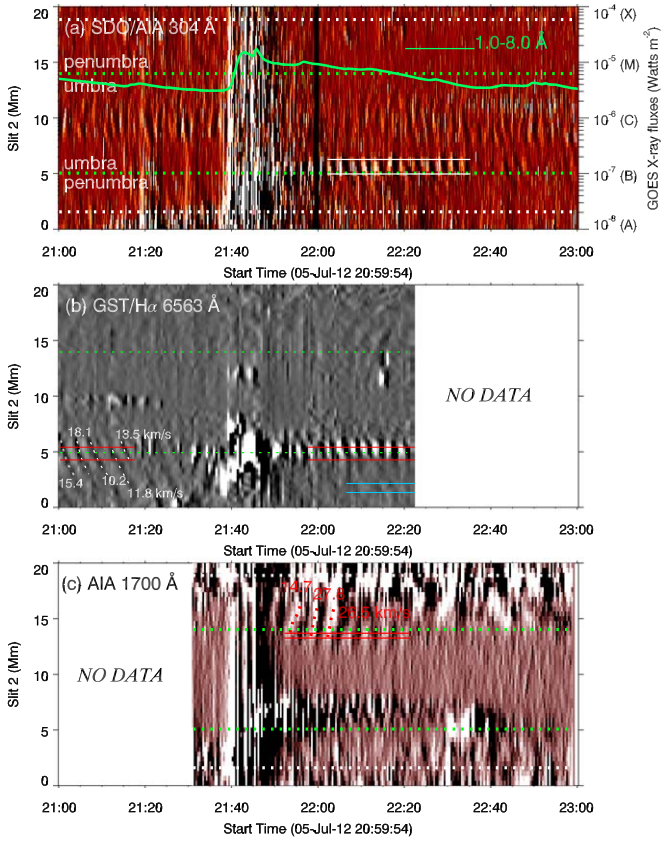

Figure 3. The time–distance plots obtained along slit 2 (the red slit shown in panel (i) of Figure 1) by stacking running-difference images in the AIA 304 Å (panel (a)), Hα 6563 Å (panel (b)), and AIA 1700 Å (panel (c)) channels. The green curve in panel (a) indicates the soft X-ray fluxes obtained in the 1–8 Å channel of GOES-15. The green dotted lines indicate the boundary between the sunspot's umbra and penumbra and the white dotted lines represent the outer boundary of the penumbra. The region of enhanced oscillation observed between 22:00 and 22:35 UT is shown by two white (red) parallel lines in the AIA 304 Å (Hα) image. The RPWs (observed, in panel (b), as gray and black stripes between the two red horizontal lines during 21:00 to 21:20 UT) propagate at a speed of 10.2−18.1 km s^{-1} before the flare onset in Hα whereas the penumbral waves are observed on the other side of the sunspot in AIA 1700 Å (observed as black and white stripes at ∼13 Mm between the two red horizontal lines during 21:50 to 22:20 UT) and propagate with speed between 14.7 and 27.8 km s^{-1}. Between each set of parallel lines in panels (a)–(c), we derived the integrated intensity. The profiles and corresponding wavelet analysis were made as shown in Figure 6.

recombination mechanism (PRM), the collisional ionization then recombination mechanism (CRM), and the collisional excitation mechanism are widely reported (e.g., Andretta & Jones 1997; Kerr et al. 2021). For the PRM (e.g., Zirin 1975; Avrett et al. 1994; Centeno et al. 2008; Leenaarts et al. 2016), coronal photons at wavelengths shorter than 504 Å penetrate into the chromosphere and photoionize helium atoms. These atoms then recombine free electrons to the excited levels of a triplet of helium atoms. For the CRM (e.g., Ding et al. 2005), nonthermal electrons can collisionally ionize the helium atom during a flare. The two processes can lead to the overpopulation of ionized helium and excited levels of triplet helium. Nonthermal collisional ionization plays an important role in the impulsive phase of a flare. However, once the temperature has increased during the flare, the thermal effect becomes more important. Thermal collisional ionization and recombination can affect the population of triplet helium (e.g., Kerr et al. 2021).

3.2. Variations of the Period and Magnetic Inclination

To investigate the effect of the flare on 3 minute oscillations, we studied the frequency changes, which are determined by the angle of the magnetic field to the local vertical and the temperature evolution, before and after the flare. The two factors can be affected by a flare. We highlight the regions where oscillation occurs by solid red, white, and blue horizontal lines in the time–distance plots in Figure 3. We created integrated intensity profiles (see Figure 6) for them, i.e., between the two horizontal solid white lines for AIA 304 Å (Figure 3, panel (a), between 22:00 and 22:35 UT), the two red lines for Hα before the flare (panel (b), between 21:00 and 21:18 UT) and after the flare (panel (b), between 22:00 and 22:21 UT), the two blue lines for Hα after the flare (panel (b), between 22:06 and 22:22 UT), and the red lines for 1700 Å (panel (c), between 21:51 and 22:20 UT). The detrended components for the integrated intensity profiles and their corresponding wavelet analysis are shown in Figure 6 for the Hα 6563 Å and AIA 304 and 1700 Å passbands. In Figure 6 panel (a2), we observe a 4 minute oscillation in the sunspot's penumbra in the AIA 1700 Å passband. In Figure 6, panels (b2) and (c2) display the periodic property before and after the flare in Hα 6563 Å. Before the flare, the period is more than 200 s. However, the period of the oscillation after the flare is 180 s, which is consistent with the period obtained in the He I 10830 Å (see Figure 2) and AIA 304 Å (see Figure 6 panel (e2)) passbands. The period of the oscillation is slightly shorter than that of the RPW at the same locations. A frequency shift is observed at He I 10830 Å, as shown in Figure 2, and presented on the integrated intensity profiles of Hα 6563 Å, as shown in Figure 6. Besides, we notice that the RPW coexists with the enhanced oscillation after the flare and the period of the RPW after the flare is the same as that before the flare, which is about 200 s, as shown in Figure 6 panels (d1)–(d3). The periods observed at various wavelengths during the pre-flare and post-flare phases are summarized in Table 3.

The 3 minute oscillation is an intrinsic property determined by the acoustic cutoff frequency in the chromospheric resonant cavity. No signal should propagate below the cutoff frequency ω_c. In an isothermal atmosphere, this is given by

$$\omega_c = \frac{\gamma g}{2c_s} = \sqrt{\frac{\gamma \mu g^2}{4RT}}, \quad (1)$$

where γ is the adiabatic index, μ is the mean molecular mass, g is the gravitational acceleration, R is the gas constant, and T is the temperature. The chromosphere would filter out frequencies less than the cutoff from the photosphere below (Lamb 1909). However, in MAG waves, the acoustic cutoff frequency that determines the period of oscillations that can propagate is given by

$$\omega_c = \frac{\gamma g \cos\theta}{2c_s} \propto \frac{g\cos\theta}{\sqrt{T}} \quad (2)$$

where θ is the angle with respect to the local vertical, and T represents the plasma temperature. The frequency is proportional to the cosine of this angle and inversely proportional to the square root of the temperature. We assume that γ remains constant.

The variation of the magnetic structure, therefore, plays an important role in the oscillation. Thus, we studied the variation

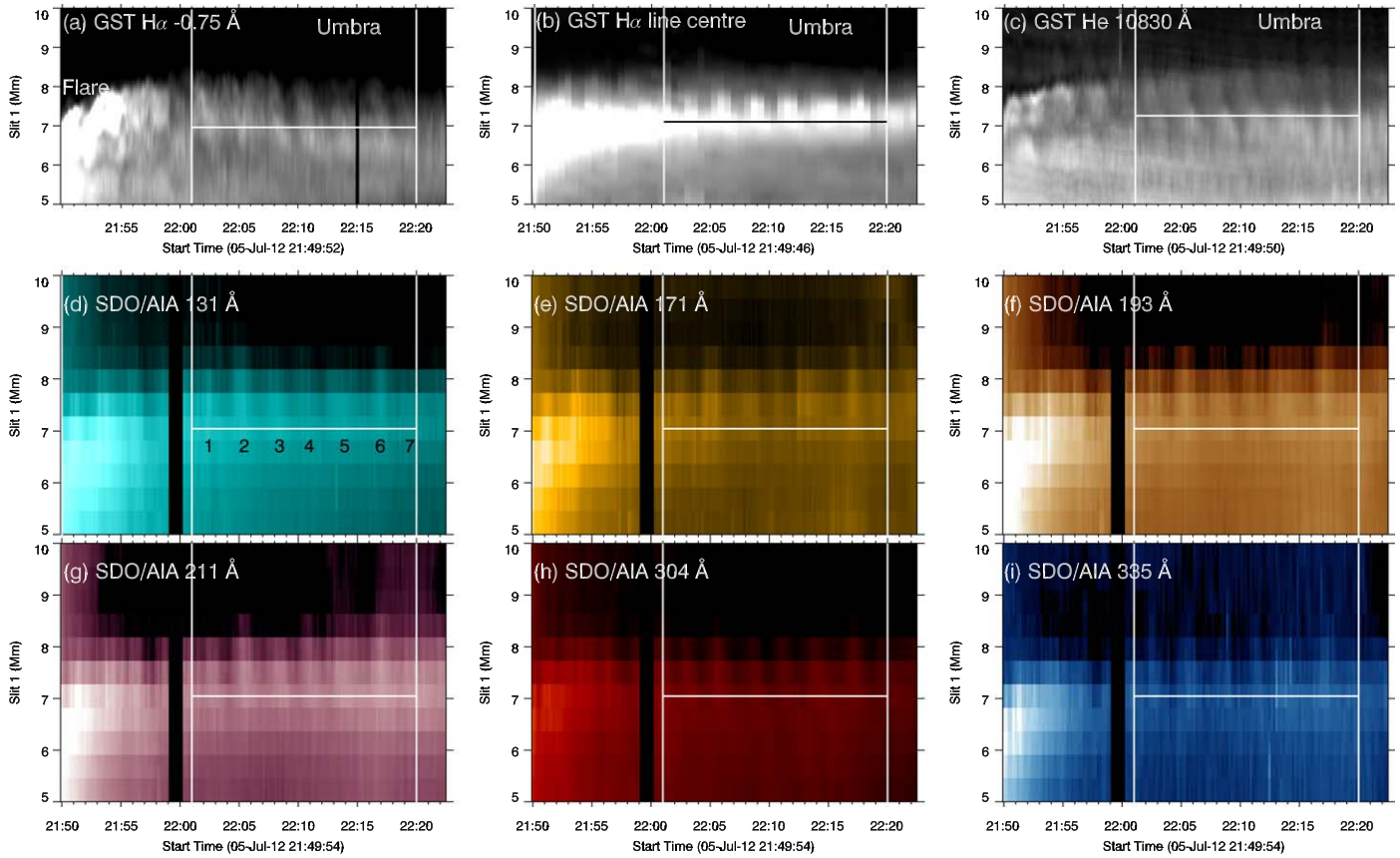

Figure 4. The time–distance plots obtained along slit 1 (shown as a white slit in panels (a)–(j) in Figure 1) by stacking intensity images in the Hα −0.75 Å, Hα 6563 Å line center, He I 10830 Å, and AIA 131, 171, 193, 211, 304, and 335 Å wavelength channels. The dark region above 8.5 Mm corresponds to the sunspot's umbra and the bright region is flare emission (see panel (a)). The oscillation contains at least seven peaks from 22:00 UT to 22:20 UT and they are labeled in panel (d). The intensity variation profiles were obtained along the white horizontal lines and are shown in Figure 5. The white vertical lines indicate the time range of the intensity variation shown in Figure 5.

of magnetic components including the magnetic field inclination from the line of sight, azimuth, and strength from 21:00 to 23:00 UT. Photospheric magnetograms were obtained from the Helioseismic and Magnetic Imager (HMI; Schou et al. 2012) on board SDO. The hmi.b_135s data series provides full-disk Milne–Eddington inversions[7] (Hoeksema et al. 2014) with magnetic field strength, inclination, azimuth, and disambiguation information at a cadence of 135 s (2 minutes 15 s). The magnetic field strength has units of Mx cm^{-2}.

In Figure 7, panel (a), we show the He I image at 21:45 UT along with 10 locations (shown as asterisks) on the umbral–penumbral boundary of the sunspot. These locations indicate regions on the oscillating stripe of the flare ribbon. Maps of the magnetic field strength, inclination, and azimuth are also shown in Figure 7 (panels (b)–(d)), and we show the time series of the magnetic field inclination and the angle with respect to the local vertical at these 10 locations in panels (e) and (f), respectively. The time series of the magnetic field azimuth and strength are shown in panels (g) and (h). The vertical solid black line indicates the flare peak time at around 21:42 UT. The two black dashed lines indicate the times 21:15 and 22:15 UT, at which we studied the emission measure (EM) distributions (see Section 3.3, Figures 9 and 10).

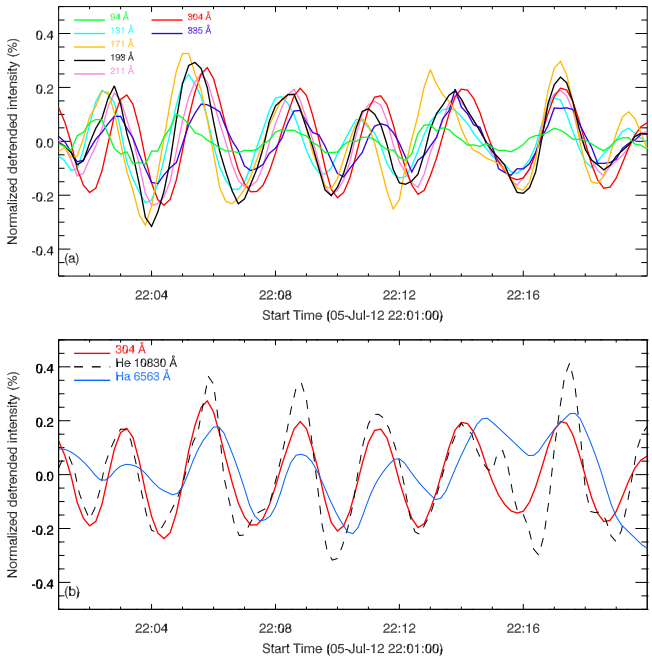

Figure 5. The intensity variation profiles for all AIA EUV passbands (top panel) and Hα and He I passbands (bottom panel) obtained along the white horizontal lines indicated in Figure 4.

[7] http://jsoc.stanford.edu/HMI/Vector_products.html

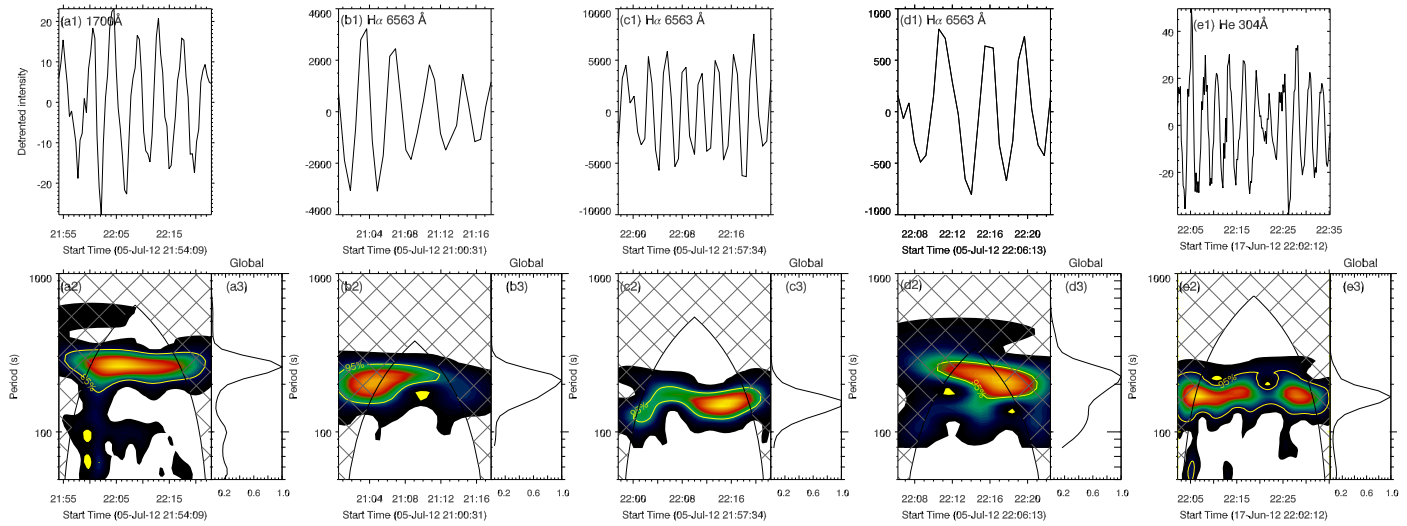

Figure 6. Top panels: the detrended component for the integrated intensity profiles obtained for the AIA 1700 Å passband (panel (a1), during the entire event), the Hα 6563 Å passband (panels (b1)–(c1), before and after the flare at the boundary of the umbra and penumbra, and panel (d1), after the flare, at the region where the RPW is still observed), and the AIA 304 Å passband (panel (e1), after the flare). These profiles are obtained for the regions shown as white, red, and blue solid lines in the time–distance plots shown in Figure 3, i.e., over the regions between the two red solid lines in AIA 1700 Å (see Figure 3 panel (c) between 21:51 and 22:20 UT), between the red and between the blue solid lines in Hα 6563 Å (see Figure 3 panel (b)), and between the white solid lines in AIA 304 Å (see Figure 3 panel (a)). Bottom panels: (a2)–(e2) Morlet wavelet power spectrum and (a3)–(e3) global wavelet power spectrum for AIA 304 and 1700 Å and Hα 6563 Å passbands at different stages during the flare.

Table 1
Time Lags between Each AIA EUV Passband

AIA	94 Å	131 Å	171 Å	193 Å	211 Å	335 Å	304 Å
94 Å	0 s	11.76 ± 1.15 s	10.9 ± 1.09 s	23.15 ± 1.56 s	29.02 ± 2.38 s	36.63 ± 1.97 s	41.89 ± 2.84 s

Over an interval of 10−20 minutes, the inclination from the line of sight of the photospheric magnetic field on the oscillating stripe decreases by up to 5° at locations 0−2 and 5−8, indicating that the magnetic field becomes more vertical. It is reasonable to assume that the chromospheric magnetic field also becomes more vertical. In contrast, the inclination at locations 3, 4, and 9 does not decrease. These three locations are possibly at the footpoint of the post-flare loop caused by the magnetic implosion or shrinkage of the post-flare loop. As seen in panel (a), locations 3, 4, and 9 are much closer to the footpoints of the post-flare loop, while the others are at the footpoints of the EUV late-phase loop, which could become more vertical.

In addition, we calculated the angle between the magnetic field and the surface normal and the results are shown in Figure 7 panel (f). These were further used for the estimation of the frequency ratio and the results are discussed in Section 3.4. The 180° ambiguity of the azimuth was solved (Hoeksema et al. 2014). The HMI vector field with components of field strength, inclination, and azimuth was converted into spherical coordinate components of *Bp*, *Bt*, and *Br* (Sun 2013). Thus, the angle with respect to the local vertical could be obtained (panel (f)). In the process of coordinate conversion, the magnetic field components (*Bp*, *Bt*, and *Br*) were dependent on the inclination, azimuth, and field strength. So, their time profiles are shown in Figure 7 as references.

3.3. Temperature Evolution

As mentioned in Section 1, the acoustic cutoff frequency is affected by the chromospheric temperature. We do not have chromospheric temperature measurements, but we can use AIA to look at the temperature evolution at transition region temperatures and above, before and after the flare. This is useful because the chromosphere, transition region, and corona are conductively linked, so this can help us understand whether the temperature structure of the chromosphere might have been changed by the flare. To obtain the temperature of the plasma at locations where the oscillation occurs, we utilized the EM method (Cheung et al. 2015). We used intensities from six AIA

Table 2
Time Lags between AIA 304 Å, He I 10830 Å, and Hα 6563 Å Passbands

	304 Å	He I 10830 Å	Hα 6563 Å
304 Å	0 s	12.79 ± 0.37 s	35.24 ± 1.57 s

Table 3
Periods Observed at Various Wavelengths during the Pre-flare and Post-flare Phases

Passbands	Pre-flare (21:00 −21:36 UT)	EUV Late Phase (21:55 −22:30 UT)
AIA 1700 Å	No data	240 s
Hα 6563 Å	∼200 s	180 s and ∼200 s
He I 10830 Å	300 s (early) and ∼200 s (late)	180 s
All EUV passbands	Invisible	180 s

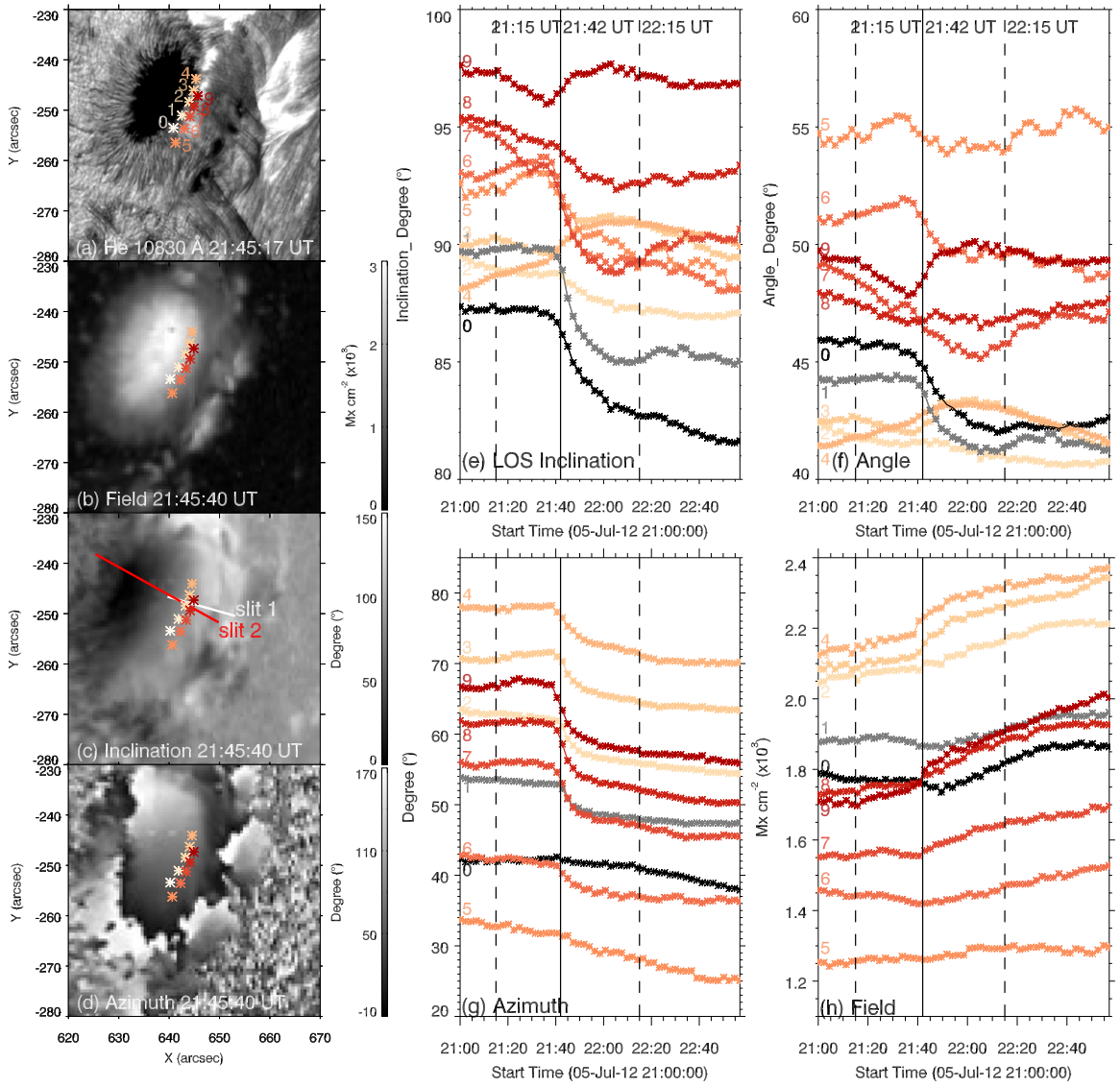

Figure 7. Panel (a) shows the He I 10830 Å image at 21:45 UT. Panels (b)–(d) show the HMI line-of-sight magnetic field strength, inclination, and azimuth, respectively. Various points in and around the sunspot umbral and penumbral boundaries are shown as colored asterisks. Panel (e) shows the time profile of the inclination of the magnetic field along the line of sight obtained at the 10 locations that are shown in the left panels. Panel (f) shows the time profile of the angle with respect to the local vertical for these locations. Panels (g) and (h) show the time profiles of the azimuth and strength of the magnetic field along the line of sight at the same 10 locations. The two black dashed vertical lines are the points before the flare at 21:15 UT and after the flare at 22:15 UT where the EM distribution and temperature are measured in Figures 9 and 10, respectively. The black solid vertical line indicates the flare's peak time, 21:42 UT. The angles with respect to the local vertical for the 10 positions at 21:15 and 22:15 UT are listed in Table 4.

coronal passbands (94, 131, 171, 193, 211, and 335 Å) in the EM analysis and obtained the EM distribution over the range of temperatures $5.4 < \log T < 7.3$. The results are shown in Figure 8. In panel (a), we show the He I image of the sunspot along with 10 locations (marked by asterisks) on the umbral–penumbral boundary of the sunspot. We studied the variations of their EM and temperature before and after the flare at 21:15 and 22:15 UT, respectively (see Figures 9 and 10). To remove the influence of data saturation and diffraction fringes during the impulsive phase and the EUV late phase, we desaturated the AIA data by using the DESAT software package[8] available in SolarSoftWare (SSW). This provided an automatic desaturation of the AIA images by using a correlation/inversion analysis of diffraction fringes produced by the telescope. The resulting EM maps at 22:15 UT in the temperature range $\log T$ [K] $\sim 5.4-5.9$ (0.25−0.8 MK) and $\log T$ [K] $\sim 6.5-7.3$ (5−19 MK) are shown in panels (b) and (c) of Figure 8, respectively. The EM values are smaller for points 0−4 compared to points 5−9 in both temperature ranges. Also, for all points, the EM values are smaller for the EM map in the temperature range of 5.4−5.9 compared to the EM map in the temperature range of 6.5−7.3.

Figures 9 and 10 compare the EM distributions of the 10 locations on the oscillating ribbon 27 minutes before the flare, at 21:15 UT, and 33 minutes after the flare, at 22:15 UT, respectively. The best-fitting EM solution of the observation is indicated by the black curves. The uncertainties on the EM solutions were measured using 100 Monte Carlo realizations of the observations. The uncertainty on the AIA intensities was calculated using the function `aia_bp_estimate_error.pro` in SSW and used in the EM analysis to obtain a 100-EM

[8] https://hesperia.gsfc.nasa.gov/ssw/packages/desat/doc/DESAT_doc.pdf

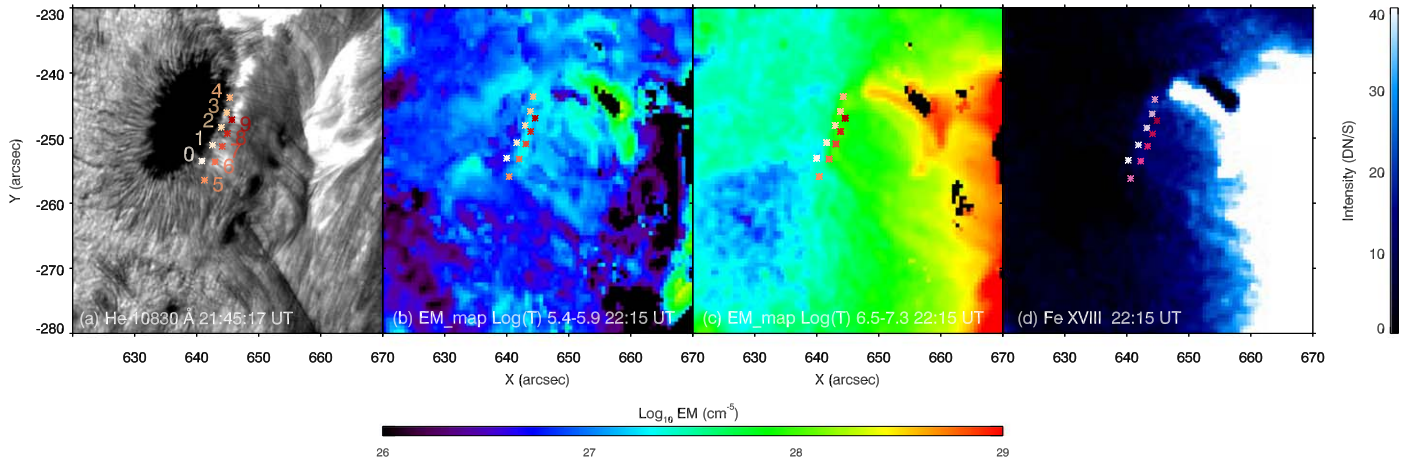

Figure 8. Panel (a): the He I 10830 Å image at 21:45:17 UT; panels (b)–(c): the EM maps created at 22:15 UT in the temperature range of log T [K] ∼ 5.4−5.9 and 6.5−7.3. The colored asterisks in all the panels indicate the 10 locations where we obtained the EM profiles as a function of temperature shown in Figures 9 and 10. The black patches (at $X = 655''$ to $658''$ and $Y = -243''$ to $-246''$) in these panels are caused by desaturation. Panel (d): Fe XVIII emission map created at 22:15 UT.

solution. These solutions are indicated as colored bars on the best-fit EM solution.

At 21:15 UT, the EM distributions for all points show two peaks, one at lower temperature, $5.5 < \log T < 5.7$ (0.3 −0.5 MK), and another at higher temperature, $6.2 < \log T < 6.5$ (1.6−3.2 MK). In the case of the late phase of the flare at 22:15 UT, we observe three peaks in the EM distribution. The first two peaks are in the same temperature range as those observed at 21:15 UT, and the third peak is observed in the very high temperature range, $\sim\log T$ [K] = 7. The long error bars in the low-temperature as well as high-temperature part of the EM distribution are indicative of the fact that the differential EM (DEM) at these temperatures is not well constrained. We obtained the EM-weighted-average temperature, $\tilde{T} = \int \mathrm{EM}(T) \times T dT \Big/ \int \mathrm{EM}(T) dT$, in the entire temperature range $5.4 < \log T < 7.3$ (0.25−19 MK). The results are summarized in Table 4. The result shows that the EM in the high-temperature range above log T [K] = 7 is enhanced at 22:15 UT. As a result, the EM-weighted-average temperature also increases. For locations 0, 5, and 6, the EMs are affected by overlying coronal loops and emission from temperatures above log T [K] = 7 is relatively weak. For the other locations 1−4 and 7−9, the EMs in the high-temperature range obviously increase. The footpoints of the late-phase loops at these locations are heated during the EUV late phase.

In order to find the validity of the high temperature ∼7 MK in the EM analysis at 22:15 UT, we carried out further analysis using three AIA channels. As stated earlier in Section 2, the AIA 94, 171, and 211 Å passbands are dominated by Fe XVIII, Fe X, and Fe XIV, respectively, during flares. We measured the contribution of Fe XVIII in 93.93 Å emission in the AIA 94 Å passband using the method by Del Zanna (2013). This method allowed us to subtract the contribution of low-temperature emission in the AIA 94 Å passband by using the low-temperature emission observed in the AIA 211 and 171 Å passbands $I(\mathrm{Fe\ XVIII}) = I(\mathrm{AIA\ 94}) - I(\mathrm{AIA\ 211})/120 - I(\mathrm{AIA\ 171})/450$. We applied this method to AIA images observed at 22:15 UT and obtained the Fe XVIII emission map that is shown in Figure 8, panel (d). This indicates there is a small amount of Fe XVIII emission available at these locations. Kindly note that the contribution function for the Fe XVIII line peaks at log T [K] = 6.85 (∼7 MK) (indicating the temperature of formation) but the line could form at a wide range of temperatures, log T [K] = 6.25 to 7.38 (2−23 MK). This does not indicate the plasma temperature we observe at 22:15 UT is ∼7 MK but it could be between 2 and 7 MK considering that the EM values at high temperatures are not well constrained by the AIA channels.

3.4. Estimation of the Frequency Ratio

To characterize the frequency change before and after the flare, we estimated the frequency ratios for different EM-weighted-average temperatures in three different temperature bands. They are $5.4 < \log T < 7.3$ ($\log \tilde{T}_{\mathrm{total}}$) for the whole temperature range; $5.4 < \log T < 6.8$ ($\log \tilde{T}_{\mathrm{total2}}$), from which we removed temperatures above log T [K] = 7.0; and a lower-temperature band, band I, $5.4 < \log T < 5.9$ ($\log \tilde{T}_{\mathrm{band}\,I}$). The frequency ratios before and after the flare were estimated by using Equation (2). In Table 4, the angle with respect to the local vertical of the photospheric magnetic field; the EM-weighted-average temperatures ($\tilde{T}$) obtained at the 10 locations in the temperature ranges $5.4 < \log T < 7.3$ ($\log \tilde{T}_{\mathrm{total}}$), $5.4 < \log T < 6.8$ ($\log \tilde{T}_{\mathrm{total2}}$), and (band I) $5.4 < \log T < 5.9$ ($\log \tilde{T}_{\mathrm{band}\,I}$); and the frequency ratios are summarized. The decrease of the angle with respect to the local vertical leads to an increase in the cutoff frequency, so the period of waves that can propagate decreases. Conversely, an increase in temperature leads to a decrease in cutoff frequency and an increase in the period. Based on the oscillation observed in the Hα 6563 Å line, the period decreases from more than 200 s of the penumbral wave to 3 minutes of the oscillation.

The estimated frequency ratios by using the low-temperature range are more consistent with the observation compared to the weighted-average temperature in the whole temperature range. We note that the temperature that determines the acoustic cutoff frequency should be the temperature in the chromosphere or temperature minimum region, which we cannot measure. However, the temperature changes, especially in the low-temperature band and in the transition region, are small. Therefore, probably, the chromospheric temperature, which is affected by the temperature change in the transition region during the late, conduction-dominated phase of the flare, changes very little.

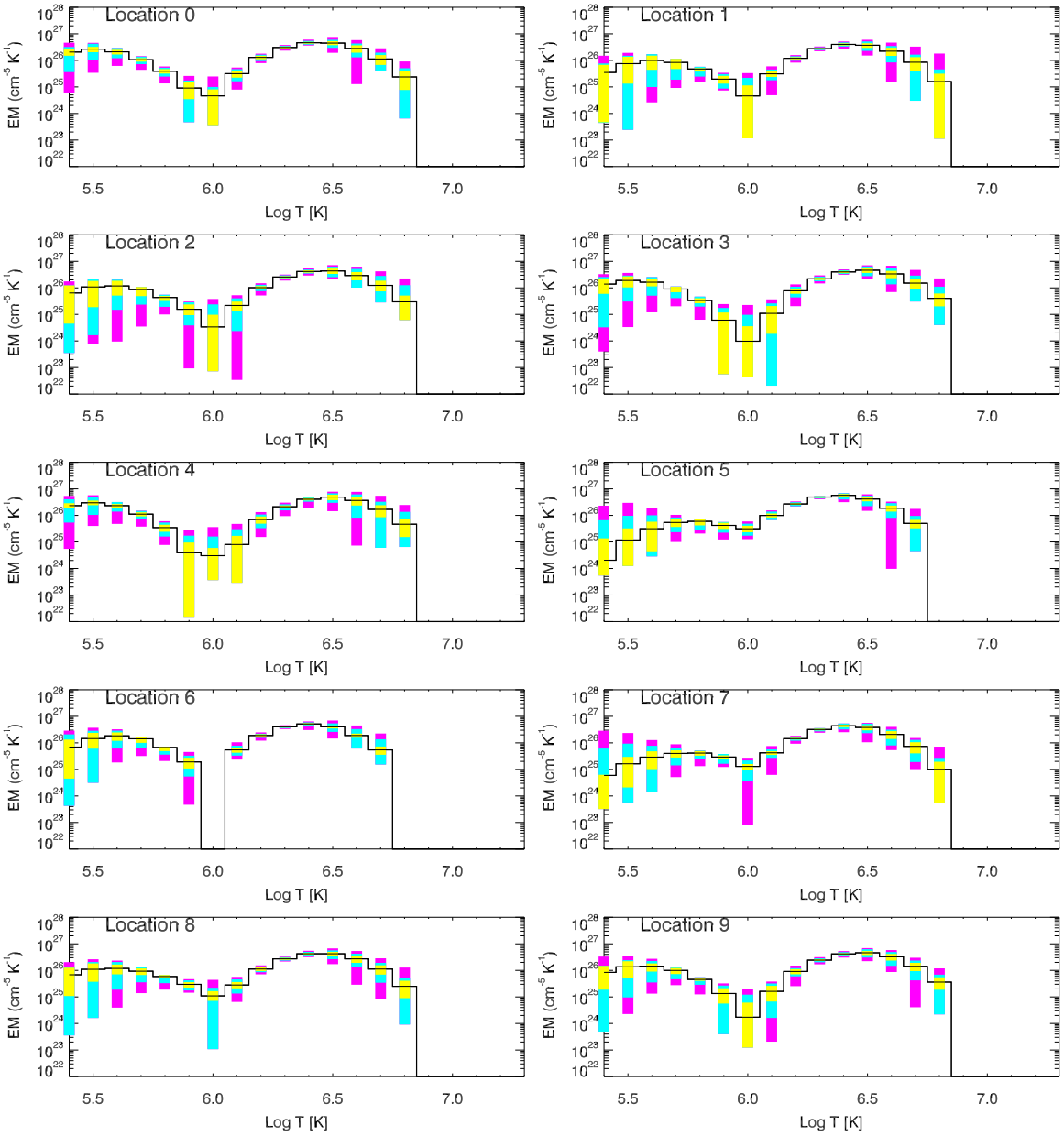

Figure 9. EM profiles at 21:15 UT (∼27 minutes before the peak of the flare) obtained at 10 locations (0–9 shown as asterisks in Figure 8). The black profiles show the best-fitted EM curves. The yellow, turquoise, and pink bars indicate the 50%, 80%, and 95% uncertainties associated with EMs that were obtained from Monte Carlo solutions.

4. Discussion and Conclusion

A thorough investigation of the M1.8-class flare observed on 2012 July 5 has been carried out by us (Wang et al. 2016, 2018, 2020) and this is the fourth part of our analysis, focusing on the enhanced 3 minute oscillation above the sunspot. This significant oscillation primarily caught our attention in He I 10830 Å images and is also unambiguously observed in the Hα 6563 Å line center, in the Hα blue wing (−0.75 Å), and at EUV wavelengths in the SDO/AIA instrument. Combining BBSO and SDO observations, EM analysis, wavelet analysis, and analysis of the magnetic components (based on SDO/HMI data), we summarize the observational findings and discuss them as follows.

During the pre-flare and post-flare phases, there are differences in oscillation periods, observed at various wavelengths, as summarized in Table 3. The He I 10830 Å emission shows periods of 300 s, ∼200 s, and 180 s for the photospheric oscillation due to the photosphere's being optically thin in the early pre-flare phase, to the RPW in the late pre-flare phase, and to the enhanced oscillation in the post-flare phase, respectively. Hα displays 200 s for the RPW before the flare and 180 s for the enhanced oscillation after the flare. Additionally, we can still see a faint RPW with a period of 200 s after the flare, which coexists with the enhanced oscillation. For all the EUV passbands, we observe the enhanced oscillation has a period of 180 s, which is consistent with the period of the enhanced oscillation observed in Hα and He I 10830 Å.

The RPW observed in the AIA 1700 Å channel, which is dominated by a continuum, shows a period of 240 s. Due to a lack of data in the AIA 1700 Å channel in the pre-flare stage, we

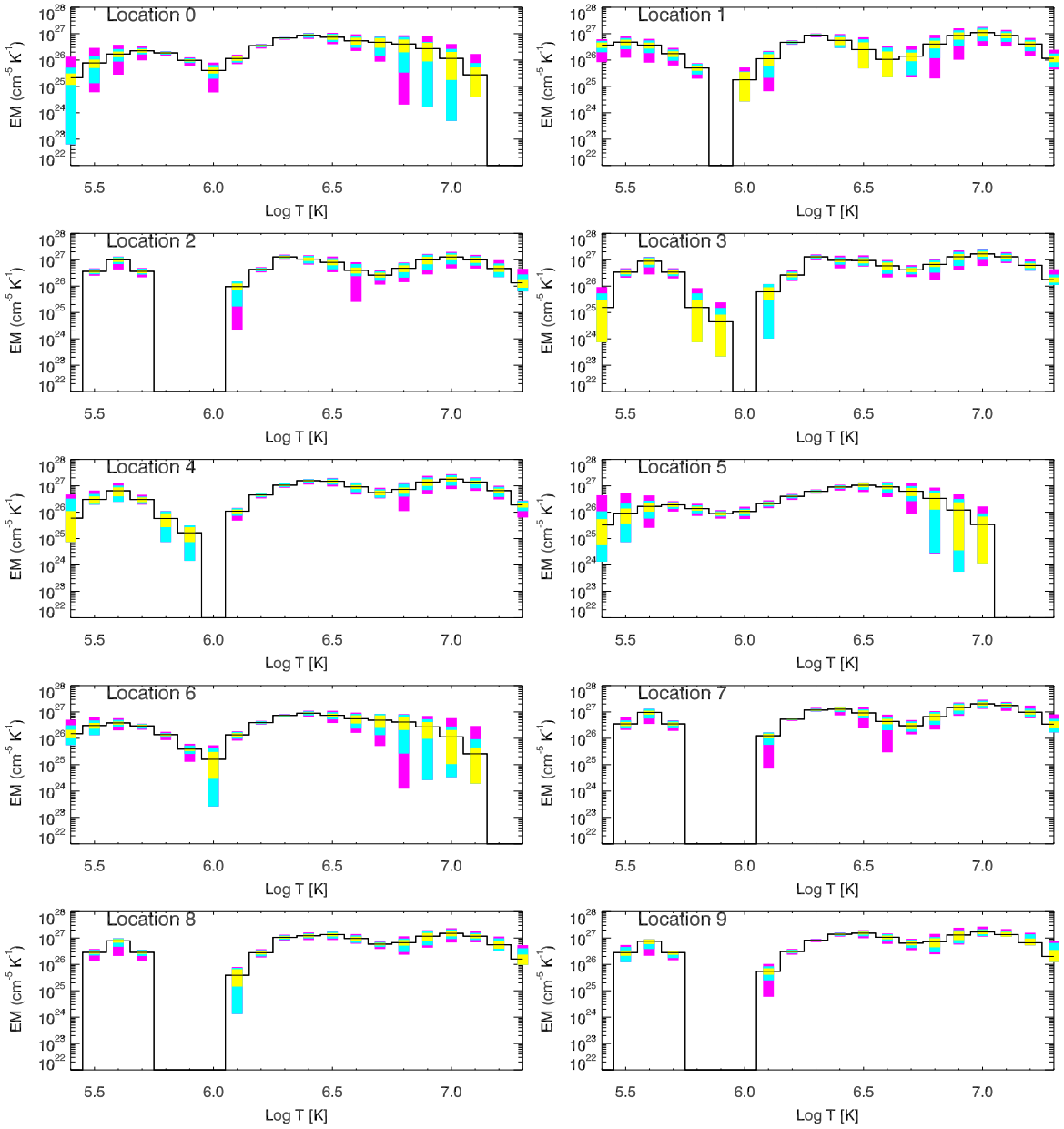

Figure 10. EM profiles at the late phase of the flare at 22:15 UT at 10 locations (0–9 shown as asterisks in Figure 8). The black profiles show the best-fitted EM curves. The yellow, turquoise, and pink bars indicate the 50%, 80%, and 95% uncertainties associated with EMs that were obtained from Monte Carlo solutions.

investigated the RPW on the opposite side of the flare-related oscillation in the sunspot. By comparison, the irregular oscillation on the eastern side, related to the flare, is also visible in AIA 1700 Å. In the same observation, the RPW detected in He I 10830 Å and Hα displays a period of above 200 s. There is only a slight difference between the two wavelengths. For the scenario supposed by, e.g., Bloomfield et al. (2007), the observed wave propagates along the magnetic field lines as a slow magnetoacoustic wave in the sunspot. The formation height is different for He I 10830 Å and Hα and the projection effect caused by the inclination of the magnetic field leads to a visually different wave pattern with different periods at different heights.

As described above, the period of the RPW changes into the 180 s period of the enhanced oscillation at the same location on the boundary of the umbra and penumbra, observed in He I 10830 Å and Hα. The period of the RPW in the time range 21:15−21:33 UT is more than 200 s, and its traveling speed is about 14.7−27.8 km s^{-1}. However, the enhanced oscillation at the footpoints of the late-phase loop between 21:55 and 22:20 UT has a shorter period of 3 minutes. In the chromospheric cavity, the magnetoacoustic cutoff frequency variation is determined by both the angle from the local vertical of the magnetic field and the temperature. By comparing the angles with respect to the local vertical of the magnetic field at 21:11 UT and 22:15 UT, we find that the angle decreases at the footpoint of the late-phase loops, for 7 out of 10 locations. With EM analysis, we find that the EM-weighted temperature of the transition region in the temperature range $5.4 < \log T < 5.9$ changes a little at 21:15 UT and 22:15 UT. We do not have a direct measurement of the chromospheric temperature profile, but we can assume that the chromospheric lines are always formed at roughly the same temperature, and the weighted-

Table 4
Angle with respect to the Local Vertical of the Photospheric Magnetic Field, Temperature from the EM Distribution, and Estimated Frequency Ratios at 10 Locations (0–9) Shown in Figure 7

Time (UT)	Properties of Locations									
		0	1	2	3	4	5	6	7	8	9
21:15	Angle with respect to local vertical (deg)	45.74	44.26	41.72	42.57	41.79	54.54	51.27	48.35	47.40	49.19
	$\log \tilde{T}_{\rm total}$ $(5.4 < \log T < 7.3)$	6.18	6.30	6.33	6.27	6.16	6.25	6.20	6.29	6.28	6.26
	$\log \tilde{T}_{\rm total2}$ $(5.4 < \log T < 6.8)$	6.18	6.30	6.32	6.26	6.16	6.25	6.20	6.29	6.27	6.26
	$\log \tilde{T}_{\rm band\,1}$ $(5.4 < \log T < 5.9)$	5.55	5.67	5.64	5.57	5.54	5.66	5.60	5.68	5.64	5.61
22:15	Angle with respect to local vertical (deg)	42.18	41.47	40.86	42.98	42.87	54.37	49.64	45.99	46.86	49.75
	$\log \tilde{T}_{\rm total}$ $(5.4 < \log T < 7.3)$	6.38	6.51	6.53	6.60	6.58	6.36	6.29	6.63	6.63	6.66
	$\log \tilde{T}_{\rm total2}$ $(5.4 < \log T < 6.8)$	6.33	6.16	6.23	6.27	6.31	6.35	6.23	6.24	6.34	6.34
	$\log \tilde{T}_{\rm band\,1}$ $(5.4 < \log T < 5.9)$	5.69	5.54	5.60	5.60	5.59	5.67	5.59	5.59	5.60	5.57
	Frequency ratio using $\log \tilde{T}_{\rm total}$	1.18	1.2	1.24	1.47	1.64	1.13	1.07	1.42	1.49	1.61
	Frequency ratio using $\log \tilde{T}_{\rm total2}$	1.12	0.81	0.88	1.02	1.22	1.11	1.01	0.91	1.07	1.11
	Frequency ratio using $\log \tilde{T}_{\rm band\,1}$	1.10	0.82	0.94	1.04	1.08	1.01	0.96	0.86	0.94	0.97

average temperature in the lowest-DEM band barely changes. So it seems likely that the change in the angle of the field with respect to the local vertical is responsible for the frequency change.

The enhanced 3 minute oscillation is observed from ∼22:00 UT to ∼22:35 UT, in the EUV late phase. The oscillation mainly occurs at the footpoints of the late-phase loop, which is located at the boundary of the sunspot's umbra and penumbra. During this time, the oscillation is observed in chromospheric lines (He I 10830 Å and Hα 6563 Å) and coronal passbands (AIA 94, 131, 171, 193, 211, and 335 Å) with the same period of around 3 minutes. There is a phase lag between passbands, with the oscillation peaking first at 94 Å, then at 131 and 171 Å, then at 193, 211, 335, and 304 Å, and at last at the He I 10830 Å and Hα passbands.

Recently, there have been studies that suggest activity from a higher layer in the atmosphere can affect the 3 minute oscillation above the sunspot, for example, plasma downflows (e.g., Kwak et al. 2016; Felipe et al. 2021). Kwak et al. (2016) reported that the weak oscillation is strongly enhanced after the downflow event and suggested that the downflow event drives the 3 minute oscillation and causes the associated heating in this region. Studies have found that an intensity increase occurs in the downflowing phase in umbral oscillations (Cho et al. 2015) and umbral flashes (Henriques et al. 2017; Bose et al. 2019). Recent numerical simulations of umbral flashes have indicated that a downflowing umbral flash is a result of the presence of standing oscillations above the sunspot umbra (Felipe et al. 2021). They have reported a scenario in which a resonant cavity produced by the sharp temperature gradient of the transition region leads to chromospheric standing oscillations.

For this study, it is interesting to identify whether the oscillation at the footpoint is also caused by standing waves, in light of recent studies revealing that umbral chromospheric waves do not propagate but instead form standing waves (Felipe et al. 2018). In addition, the enhanced oscillation is observed during the EUV late phase when there is additional heating, and downflow is also clearly observed. Considering that we can still observe a faint RPW during almost the same time as the enhanced oscillation, and that the 3 minute oscillation is the inherent frequency in the chromosphere, we suggest that the enhanced oscillation with a back-and-forth pattern, in which frequency is determined by the acoustic cutoff frequency in the chromospheric cavity, is affected by the additional heating, maybe related to the downflow. To explore more physical explanations of the enhanced 3 minute oscillation and the propagating property, a further simulation study is expected.

Acknowledgments

We thank the anonymous referee for constructive comments and suggestions. This work is supported by the National Key R&D Program of China 2021YFA1600502 (2021YFA1600500); the Strategic Priority Research Program of the Chinese Academy of Sciences, grant No. XDB 0560000 (XDB0560102); and NSFC grants 12003072, 12173092, 12073081, 12273115, and 12273101. S.M. and L.F. acknowledge support from UK Research and Innovation's Science and Technology Facilities Council under grant award Nos. ST/T000422/1 and ST/X000990/1. Y.W. is supported by the China Scholarship Council and the Youth Fund of JiangSu No. BK20191108. W.C. acknowledges support from US NSF grants—AGS-2309939, AGS-1821294, and AST-2108235. We thank Dr. Jianping Li for helpful discussions. We thank the team of SDO/AIA and SDO/HMI for providing valuable data. The AIA and HMI data were downloaded via the Joint Science Operations Center. We gratefully acknowledge our use of data from GST of BBSO. BBSO operation is supported by the US NSF AGS-2309939 and AGS-1821294 grants and the New Jersey Institute of Technology. GST operation is partly supported by the Korea Astronomy and Space Science Institute and Seoul National University.

Appendix

Figure A1 in the Appendix shows the Hα image and the time-distance plots along a slit, displaying the running penumbra wave before the flare, and the coexistence of the running penumbral wave and the enhanced oscillation after the flare.

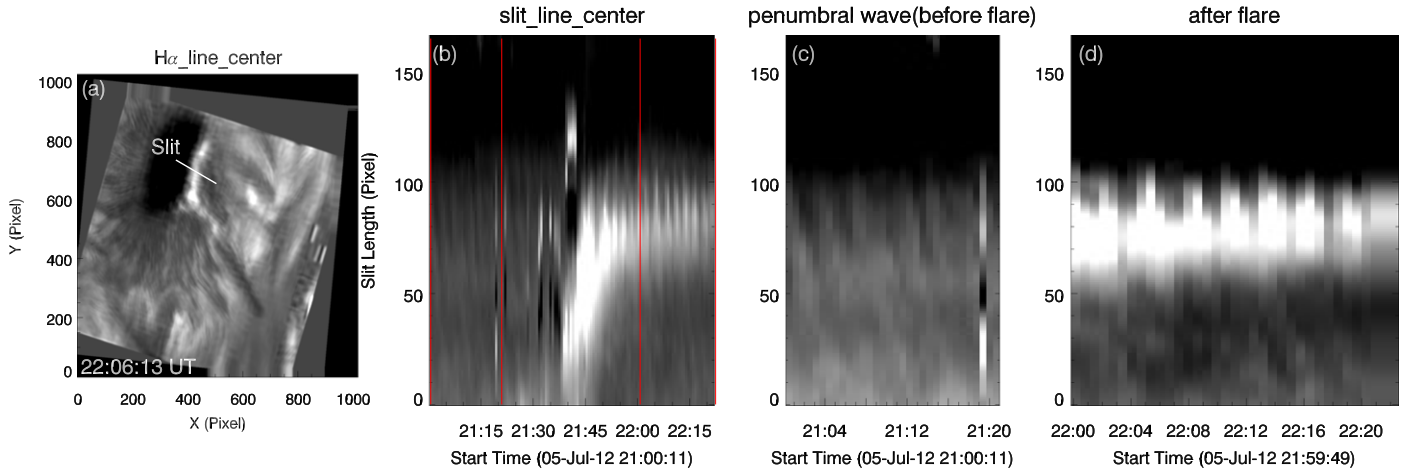

Figure A1. The evolution of the sunspot's umbral–penumbral boundary region in the Hα line center where the enhanced oscillation and penumbral wave coexist during 22:00 to 22:20 UT. Panel (a) shows the Hα image at the line center at 22:06:13 UT. The white line indicates the slit position along which we created the time–distance plots that are shown in the other panels. Panel (b): the oscillation at the boundary of the umbra and penumbra over the whole event from 21:00 to 22:20 UT. The regions highlighted with two red rectangles indicate the regions shown in panels (c) and (d). Panel (c): the gray and black stripes indicate the penumbral wave before the flare. Panel (d): the coexistence of the enhanced oscillation and penumbral wave after the flare from 22:00 to 22:20 UT.

ORCID iDs

Ya Wang https://orcid.org/0000-0003-3699-4986
Lyndsay Fletcher https://orcid.org/0000-0001-9315-7899
Sargam Mulay https://orcid.org/0000-0002-9242-2643
Haisheng Ji https://orcid.org/0000-0002-5898-2284
Wenda Cao https://orcid.org/0000-0003-2427-6047

References

Abdelatif, T. E., Lites, B. W., & Thomas, J. H. 1986, ApJ, 311, 1015
Andretta, V., & Jones, H. P. 1997, ApJ, 489, 375
Auchère, F., Froment, C., Bocchialini, K., Buchlin, E., & Solomon, J. 2016, ApJ, 825, 110
Avrett, E. H., Fontenla, J. M., & Loeser, R. 1994, in IAU Symp. 154, Infrared Solar Physics, ed. D. M. Rabin, J. T. Jefferies, & C. Lindsey (Dordrecht: Kluwer), 35
Balthasar, H., Schleicher, H., Bendlin, C., & Volkmer, R. 1996, A&A, 315, 603
Beckers, J. M., & Tallant, P. E. 1969, SoPh, 7, 351
Bel, N., & Leroy, B. 1977, A&A, 55, 239
Bloomfield, D. S., Lagg, A., & Solanki, S. K. 2007, ApJ, 671, 1005
Bogdan, T. J., & Judge, P. G. 2006, RSPTA, 364, 313
Bose, S., Henriques, V. M. J., Rouppe van der Voort, L., & Pereira, T. M. D. 2019, A&A, 627, A46
Botha, G. J. J., Arber, T. D., Nakariakov, V. M., & Zhugzhda, Y. D. 2011, ApJ, 728, 84
Braun, D. C., Duvall, T. L. J., & Labonte, B. J. 1988, ApJ, 335, 1015
Centeno, R., Collados, M., & Trujillo Bueno, J. 2006, ApJ, 640, 1153
Centeno, R., Trujillo Bueno, J., Uitenbroek, H., & Collados, M. 2008, ApJ, 677, 742
Cheung, M. C. M., Boerner, P., Schrijver, C. J., et al. 2015, ApJ, 807, 143
Cho, K. S., Bong, S. C., Nakariakov, V. M., et al. 2015, ApJ, 802, 45
Del Zanna, G. 2013, A&A, 558, A73
Ding, M. D., Li, H., & Fang, C. 2005, A&A, 432, 699
Felipe, T. 2019, A&A, 627, A169
Felipe, T., Henriques, V. M. J., de la Cruz Rodríguez, J., & Socas-Navarro, H. 2021, A&A, 645, L12
Felipe, T., & Sangeetha, C. R. 2020, A&A, 640, A4
Felipe, T., Socas-Navarro, H., & Przybylski, D. 2018, A&A, 614, A73
Fleck, B., & Schmitz, F. 1991, A&A, 250, 235
Goode, P. R., & Cao, W. 2012, Proc. SPIE, 8444, 844403
Goode, P. R., Coulter, R., Gorceix, N., Yurchyshyn, V., & Cao, W. 2010, AN, 331, 620
Hayes, L. A., Gallagher, P. T., Dennis, B. R., et al. 2019, ApJ, 875, 33
Henriques, V. M. J., Mathioudakis, M., Socas-Navarro, H., & de la Cruz Rodríguez, J. 2017, ApJ, 845, 102
Hoeksema, J. T., Liu, Y., Hayashi, K., et al. 2014, SoPh, 289, 3483
Jess, D. B., Snow, B., Fleck, B., Stangalini, M., & Jafarzadeh, S. 2021, NatAs, 5, 5
Jess, D. B., Snow, B., Houston, S. J., et al. 2020, NatAs, 4, 220
Kerr, G. S., Xu, Y., Allred, J. C., et al. 2021, ApJ, 912, 153
Kobanov, N. I., & Makarchik, D. V. 2004, A&A, 424, 671
Kosovichev, A. G., & Sekii, T. 2007, ApJL, 670, L147
Kupriyanova, E., Kolotkov, D., Nakariakov, V., & Kaufman, A. 2020, STP, 6, 3
Kwak, H., Chae, J., Song, D., et al. 2016, ApJL, 821, L30
Lamb, H. 1909, Proc. London Math. Soc., 2, 122
Leenaarts, J., Golding, T., Carlsson, M., Libbrecht, T., & Joshi, J. 2016, A&A, 594, A104
Lemen, J. R., Title, A. M., Akin, D. J., et al. 2012, SoPh, 275, 17
Li, D., Feng, S., Su, W., & Huang, Y. 2020, A&A, 639, L5
Li, D., Ge, M., Dominique, M., et al. 2021, ApJ, 921, 179
Marmolino, C., & Stebbins, R. T. 1989, MmSAI, 60, 71
Millar, D. C. L., Fletcher, L., & Milligan, R. O. 2021, MNRAS, 503, 2444
Milligan, R. O., Fleck, B., Ireland, J., Fletcher, L., & Dennis, B. R. 2017, ApJL, 848, L8
Nakariakov, V. M., Foullon, C., Verwichte, E., & Young, N. P. 2006, A&A, 452, 343
Nakariakov, V. M., & Melnikov, V. F. 2009, SSRv, 149, 119
Nye, A. H., & Thomas, J. H. 1974, SoPh, 38, 399
O'Dwyer, B., Del Zanna, G., Mason, H. E., Weber, M. A., & Tripathi, D. 2010, A&A, 521, A21
Pesnell, W. D., Thompson, B. J., & Chamberlin, P. C. 2012, SoPh, 275, 3
Priya, T. G., Wenda, C., Jiangtao, S., et al. 2018, ApJ, 852, 15
Schou, J., Scherrer, P. H., Bush, R. I., et al. 2012, SoPh, 275, 229
Simões, P. J. A., Reid, H. A. S., Milligan, R. O., & Fletcher, L. 2019, ApJ, 870, 114
Sun, X. 2013, arXiv:1309.2392
Sych, R., & Nakariakov, V. M. 2014, A&A, 569, A72
Sych, R., Nakariakov, V. M., Karlicky, M., & Anfinogentov, S. 2009, A&A, 505, 791
Torrence, C., & Compo, G. P. 1998, BAMS, 79, 61
Ulrich, R. K. 1970, ApJ, 162, 993
Wang, Y., Ji, H., Warmuth, A., Li, Y., & Cao, W. 2020, ApJ, 905, 126
Wang, Y., Su, Y., Hong, Z., et al. 2016, ApJ, 833, 250
Wang, Y., Su, Y., Shen, J., et al. 2018, ApJ, 859, 148
Woods, T. N., Eparvier, F. G., Hock, R., et al. 2012, SoPh, 275, 115
Woods, T. N., Hock, R., Eparvier, F., et al. 2011, ApJ, 739, 59
Zhugzhda, Y. D. 2008, SoPh, 251, 501
Zimovets, I. V., McLaughlin, J. A., Srivastava, A. K., et al. 2021, SSRv, 217, 66
Zirin, H. 1975, ApJL, 199, L63
Zirin, H., & Stein, A. 1972, ApJL, 178, L85